Ab Initio Theory of Fourier-Transformed Quasiparticle Interference Maps and Application to the Topological Insulator Bi_2Te_3

Philipp Rüßmann,* Phivos Mavropoulos, and Stefan Blügel

The quasiparticle interference (QPI) technique is a powerful tool that allows to uncover the structure and properties of electronic structure of a material combined with scattering properties of defects at surfaces. Recently, this technique has been pivotal in proving the unique properties of the surface state of topological insulators which manifests itself in the absence of backscattering. Herein, a Green function-based formalism is derived for the ab initio computation of Fourier-transformed QPI images. The efficiency of the new implementation is shown at the examples of QPI that forms around magnetic and nonmagnetic defects at the Bi_2Te_3 surface. This method allows a deepened understanding of the scattering properties of topologically protected electrons off defects and is a useful tool in the study of quantum materials in the future.

1. Motivation

The scanning tunneling microscopy (STM) experiments of Crommie et al.[1] and Hasegawa and Avouris,[2] revealing standing density waves of the Cu(111) and Au(111) surface-state electrons near defects, have pioneered a very powerful, direct method of imaging the surface electron liquid of metals. Together with scanning tunneling spectroscopy (STS), the method gives unique insight on the quasiparticle interference (QPI), scattering phase shifts, and lifetime. Especially when augmented by the Fourier-transformed QPI map, as proposed by Petersen et al.,[3] the method unveils scattering properties of quasiparticles off surface defects, giving information on the

scattering vectors among points of the band structure. In this context, Fourier-transformed QPI maps provided one of the first experimental proofs of the existence of topological insulators,[4] because it revealed the "absence" of intensity at back-scattering vectors, just as predicted by theory.

From a theoretical point of view, the calculation of QPI maps has been largely based on model methods, e.g., on topological insulator surfaces,[5] where the surface band structure can be approximated by simple model Hamiltonians. In general, however, density-functional-based methods are necessitated for a realistic description of the surface electronic structure and in particular of the impurity potential, where the charge relaxation around the impurity plays a major role in the correct description of the scattering phase shifts. A difficulty in density-functional calculations is that the density oscillations induced by the defect are very long-ranged, reaching tens or even hundreds of nanometers, so that supercell methods cannot practically reach this limit. These challenges can only be met by ab initio Green function embedding methods, like the Korringa–Kohn–Rostoker (KKR) method.

As an example of an application, we refer to the calculations by Lounis et al.[6] of QPI on Cu(111) and Cu(001) surfaces due to an isolated impurity buried under the surface. These results show that ab initio calculations of QPI maps over quite large surface areas are feasible with Green function techniques. However, in the case of Fourier-transformed QPI map, it is practical to express the result directly by a convolution of Green functions,[7] avoiding the intermediate step of calculating the real-space map in a large surface area.

In this article, we approach this problem and give applications in the field of topological insulators. In Section 2, we outline the formalism for real-space and Fourier-transformed QPI maps within the KKR method. Furthermore, we discuss the Fourier-transformed QPI for the practical case of multiple impurities and argue that the many-impurity problem is well approximated by the single-impurity result. We also discuss the extended joint density of states approach (exJDOS). In Section 3, we apply our formalism on the topological insulator Bi_2Te_3 with surface impurities. This is implemented in the JuKKR code package.[8] Finally, we conclude with a summary in Section 4.

Dr. P. Rüßmann, Prof. S. Blügel
Peter Grünberg Institut and Institute for Advanced Simulation
Forschungszentrum Jülich and JARA
D-52425 Jülich, Germany
E-mail: P.Ruessmann@fz-juelich.de

Prof. P. Mavropoulos
Department of Physics
National and Kapodistrian University of Athens
Zografou, Athens GR-15784, Greece

2. Formalism

Within the Tersoff–Hamann approximation,[9] the STM differential tunneling conductivity at a bias voltage U is related to the space- and energy-resolved density of states $n(r; E)$ at energy E and at the position r of the tip: $n(r; E_{\mathrm{F}} + eU) \propto \frac{\mathrm{d}I}{\mathrm{d}U}(U)$ (E_{F} is the Fermi level). In a QPI experiment, we are interested in the difference of density induced by an impurity with respect to the pristine host surface,

$$\Delta n(r; E) = n^{\mathrm{imp}}(r; E) - n^{\mathrm{host}}(r; E) \tag{1}$$

2.1. Green Function and $\mathcal{T}$-Matrix Approach

The Green function and $\mathcal{T}$-matrix approach is a well-established method of calculating the density of systems with impurities. It has been applied to the QPI problem in ab initio and model calculations, e.g., the studies by Lee et al., Wang and Lee, and Guo and Franz.[5,7,10] Herein, we give the formalism in an explicit real-space representation, because it forms the basis of the formalism and discussion in subsequent sections.

The difference in the local density of states is connected to the one-electron Green function of the system with impurity, $G^{\mathrm{imp}}(r, r'; E)$, and to the one of the pristine host, $G^{\mathrm{host}}(r, r'; E)$, by the well-known identity

$$\Delta n(r; E) = -\frac{1}{\pi} \mathrm{ImTr}[G^{\mathrm{imp}}(r, r; E) - G^{\mathrm{host}}(r, r; E)] \tag{2}$$

The trace is implied with respect to spin indices; in the case of a relativistic formalism with Dirac four-vector states, the trace includes also the large and small components. By virtue of the Dyson equation, $G^{\mathrm{imp}} - G^{\mathrm{host}} = G^{\mathrm{host}} \Delta V G^{\mathrm{imp}} = G^{\mathrm{imp}} \Delta V G^{\mathrm{host}}$, the difference in the Green function $\Delta G = G^{\mathrm{imp}} - G^{\mathrm{host}}$ is written as

$$\Delta G(r, r; E) = \int d^3 r' \int d^3 r'' G^{\mathrm{host}}(r, r'; E) \mathcal{T}(r', r''; E) G^{\mathrm{host}}(r'', r; E) \tag{3}$$

in terms of the $\mathcal{T}$-matrix,

$$\mathcal{T}(r', r''; E) = \Delta V(r')\delta(r' - r'') + \Delta V(r') G^{\mathrm{imp}}(r', r''; E) \Delta V(r'') \tag{4}$$

$\Delta V = V^{\mathrm{imp}} - V^{\mathrm{host}}$ is the difference in the potential between the impurity and host systems. The $\mathcal{T}$-matrix has the advantage that it is confined in the small region where the potential difference does not vanish and has to be calculated only once, irrespective of the range of r in the QPI calculation. For the calculation of G^{host}, the translational invariance of the surface allows us to use the Bloch theorem. Decomposing the position vector as $r = R + x$, where R is a lattice translation vector parallel to the surface plane, whereas x is a vector in the primitive cell, we write

$$G^{\mathrm{host}}(R + x, R' + x'; E) = \frac{1}{\Omega_{\mathrm{rec}}} \int d^2 k\, G_k^{\mathrm{host}}(x, x'; E) e^{ik \cdot (R - R')} \tag{5}$$

where the Fourier-transform of the Green function obeys the spectral representation

$$G_k^{\mathrm{host}}(x, x'; E) = \sum_\alpha \frac{\Psi_{\alpha k}(x)\Psi_{\alpha k}^\dagger(x')}{E - E_{\alpha k} + i0} \tag{6}$$

Here, $\Psi_{\alpha k}$ is the host wavefunction, α is the band index, $\Omega_{\mathrm{rec}} = (2\pi)^2/\Omega_{\mathrm{cryst}}$, with Ω_{cryst} the total crystal surface area, and $i0$ represents an infinitesimal imaginary energy. The difference in Green functions, Equation (3), takes then the form

$$\Delta G(R + x, R + x; E)$$

$$= \frac{1}{\Omega_{\mathrm{rec}}^2} \int d^2 k \int d^2 k' e^{i(k-k') \cdot R} \sum_{R', R''} \int_{R'} d^3 x'$$

$$\times \int_{R''} d^3 x'' e^{-ik \cdot R'} e^{ik' \cdot R''} G_k^{\mathrm{host}}(x, x'; E)$$

$$\times \mathcal{T}(R' + x', R'' + x''; E) G_{k'}^{\mathrm{host}}(x'', x; E) \tag{7}$$

$$= \frac{1}{\Omega_{\mathrm{rec}}^2} \int d^2 k \int d^2 k' \sum_{\alpha \alpha'} \frac{\Psi_{\alpha k}(x) \mathcal{T}_{\alpha k \alpha' k'}(E) \Psi_{\alpha' k'}^\dagger(x)}{(E - E_{\alpha k} + i0)(E - E_{\alpha' k'} + i0)} e^{i(k-k') \cdot R} \tag{8}$$

The sum over R', R'' and the integration over $d^3 x'$, $d^3 x''$ is confined to the sites where the $\mathcal{T}$-matrix (and the impurity perturbation ΔV) is nonvanishing. The former expression, Equation (7), includes phase factors $e^{-ik \cdot R'} e^{ik' \cdot R''}$ for the interlattice-site propagation of the host Green function, when the impurity spreads over many lattice sites. The latter expression (8) is a more compact form where the matrix elements $\mathcal{T}_{\alpha k \alpha' k'}(E) = (\Psi_{\alpha k}, \mathcal{T}(E)\Psi_{\alpha' k'})$ were introduced (note that the summation includes all states, not just the ones at energy E). It leads to the stationary phase approximation[6] pinning the energy to the energy-shell E, if the observation point is far from the impurity ($|R| \to \infty$).

For the Fourier-transformed QPI, we need the Fourier transformation of the Green function along a surface parallel to, and at vertical distance z from, the crystal surface:

$$\Delta G(z; q; E) = \int_{(z)} d^2 r \Delta G(r, r; E) e^{-iq \cdot r} \tag{9}$$

$$= \frac{\Omega_{\mathrm{BZ}}}{\Omega_{\mathrm{rec}}^2} \int_{(z)} d^2 x e^{-iq \cdot x} \int d^2 k \sum_{R' R''} e^{-ik \cdot R'} e^{i(k-q) \cdot R''}$$

$$\times \int_{R'} d^3 x' \int_{R''} d^3 x'' G_k^{\mathrm{host}}(x, x'; E)$$

$$\times \mathcal{T}(R' + x', R'' + x''; E) G_{k-q}^{\mathrm{host}}(x'', x; E) \tag{10}$$

In the step from (9) to (10), we used Equation (7), and we removed lattice sum $\sum_R$ by virtue of the identity $\sum_R e^{i(k-k'-q)R} = \Omega_{\mathrm{BZ}} \delta(k - k' - q)$ (Ω_{BZ} is the surface Brillouin zone area). The result represents the convolution of two Green functions, as expected from the Fourier transform of their products. Using Equation (2), we arrive at the following expression for the Fourier transformed QPI

$$\Delta n(z; q; E) = \int_{(z)} d^2 r\, n(r; E) e^{-iq \cdot r}$$

$$= -\frac{1}{2i\pi} \mathrm{Tr}[\Delta G(z; q; E) - \Delta G(z; -q; E)^*] \tag{11}$$

where it is implied that the complex conjugation operation ΔG^* is done after the Fourier transformation. This result can easily be generalized for the spin density with $\sigma \Delta G$ in the place of ΔG (σ is the vector of Pauli matrices).

The strongest density change measured by the STM is induced directly "above the impurity," i.e., at a vertical distance $z > 0$ from the position where $\Delta V \neq 0$. This region is often excluded in from the Fourier transformation in experiment,[11] otherwise the image is dominated by the transform of the impurity shape,[12] while one seeks the scattering vectors. In addition, the region close to the impurity is also excluded sometimes, because it may produce spurious background effects in the experiment.[13,14] In the calculation, the contribution of the excluded region (indicated by Ω_{excl}) must be subtracted explicitly, because the form (10) already includes a summation over all lattice sites. Thus we define

$$\Delta \check{n}(z; \boldsymbol{q}; E) = \Delta n(z; \boldsymbol{q}; E) - \int_{\Omega_{\text{excl}}} d^2 r n(z; \boldsymbol{q}; E) e^{-i\boldsymbol{q}\cdot\boldsymbol{r}} \quad (12)$$

$$= \Delta n(z; \boldsymbol{q}; E) + \frac{1}{\pi} \text{ImTr} \int_{\Omega_{\text{excl}}} d^2 r \Delta G(\boldsymbol{r}, \boldsymbol{r}; E) e^{-i\boldsymbol{q}\cdot\boldsymbol{r}} \quad (13)$$

However, as Ω_{excl} is finite-sized, the integration is straightforward in real space.

2.2. Expression in the KKR Formalism

In the KKR method, the Green function is expanded in site-dependent scattering wavefunctions at sites n. The vacuum is also described in a site-centered way by a continuation of the lattice structure beyond the surface, with the corresponding "empty sites" containing no atoms but a finite electron density. We denote the general position by $\boldsymbol{r} = \boldsymbol{X}_n + \boldsymbol{x} = \boldsymbol{R}_i + \chi_\mu + \boldsymbol{x}$, where the combined index $n = (i; \mu)$ defines a site $\boldsymbol{X}_n$ by the lattice-vector $\boldsymbol{R}_i$ and the sub-lattice vector χ_μ, and where $\boldsymbol{x}$ is a position vector in the atomic site with respect to the site center. We use the regular, $\mathcal{R}_L^n(\boldsymbol{x}; E)$, and irregular, $\mathcal{H}_L^n(\boldsymbol{x}; E)$, solutions of the scattering problem of the potential in the vicinity of the site $\boldsymbol{R}_n$, where L comprises angular momentum and spin indices of the incoming wave. $\mathcal{R}_L^n$ and $\mathcal{H}_L^n$ are (2×1) column vectors in Pauli–Schrödinger theory and (4×1) column vectors in Dirac theory. Also, the corresponding left-hand side solutions are required, denoted by $\bar{\mathcal{R}}_L^n(\boldsymbol{x}; E)$ and $\bar{\mathcal{H}}_L^n(\boldsymbol{x}; E)$, respectively, that are row vectors. The expansion breaks the Green function down into a single-site term and a multiple scattering term,

$$G(\boldsymbol{X}_n + \boldsymbol{x}, \boldsymbol{X}_{n'} + \boldsymbol{x}'; E) = \sum_L G_{S L}^n(\boldsymbol{x}, \boldsymbol{x}'; E)\delta_{nn'}$$

$$+ \sum_{LL'} G_{M LL'}^{nn'}(\boldsymbol{x}, \boldsymbol{x}'; E)$$

$$= -i\kappa \sum_L \Big[\mathcal{R}_L^n(\boldsymbol{x}; E)\bar{\mathcal{H}}_L^n(\boldsymbol{x}'; E)\theta(x' - x) \quad (14)$$

$$+ \mathcal{H}_L^n(\boldsymbol{x}; E)\bar{\mathcal{R}}_L^n(\boldsymbol{x}'; E)\theta(x - x')\Big]\delta_{nn'}$$

$$+ \sum_{LL'} \mathcal{R}_L^n(\boldsymbol{x}; E)\mathcal{G}_{LL'}^{nn'}(E)\bar{\mathcal{R}}_{L'}^{n'}(\boldsymbol{x}'; E)$$

where $\kappa = (2mE)^{1/2}/\hbar$ in Pauli–Schrödinger theory and $\kappa = (2mE + E^2/c^2)^{1/2}/\hbar$ in Dirac theory. The single-site term describes the Green function of the potential at site n embedded in free space. It only depends on the local potential and its contribution to ΔG vanishes outside the impurity region. The second term describes the multiple scattering over all sites, expressed by the structural Green function coefficients $\mathcal{G}_{LL'}^{nn'}(E)$. These form a matrix $[\![\mathcal{G}(E)]\!]$ that obeys an algebraic Dyson equation. This reads for the host system

$$[\![\mathcal{G}^{\text{host}}(\boldsymbol{k}; E)]\!] = [\![g(\boldsymbol{k}; E)]\!] + [\![g(\boldsymbol{k}; E)]\!] [\![t^{\text{host}}(E)]\!] [\![\mathcal{G}^{\text{host}}(\boldsymbol{k}; E)]\!]$$

$$(15)$$

where we have expressed everything in reciprocal space. $[\![g(\boldsymbol{k}; E)]\!]$ contains the structural Green function coefficients of free space and $[\![t^{\text{host}}(E)]\!]$ is a site-diagonal ($\boldsymbol{k}$-independent) matrix containing the $\mathcal{T}$-matrices of each site with respect to free space, $t_{LL'}^{\text{host};\mu}(E)$, expressed in an angular momentum and spin basis. The lattice part of the Fourier transformation affects only the structural Green functions $[\![\mathcal{G}^{\text{host}}(\boldsymbol{k}; E)]\!]$, not the $\mathcal{T}$-matrices or local scattering solutions.

The analogon of the $\mathcal{T}$-matrix in the KKR method is the *scattering path operator* of the impurity with respect to the host, $[\![\tau(E)]\!]$. It is expressed in terms of the single-site $\mathcal{T}$-matrices of impurity and host, $\Delta t_{LL'}^n(E) = t_{LL'}^{\text{imp};n}(E) - t_{LL'}^{\text{host};n}(E)$, and of the host structural Green function, by the Dyson-type equation $[\![\tau]\!] = [\![\Delta t]\!] + [\![\Delta t]\!] [\![\mathcal{G}^{\text{host}}]\!] [\![\tau]\!]$. It is not site-diagonal, and has nonvanishing elements $\tau_{LL'}^{nn'}(E)$ only between sites (n, n') for which $\Delta t^n \neq 0$ and $\Delta t^{n'} \neq 0$. The structural Green function of the system with impurity is then expressed by

$$\mathcal{G}_{LL'}^{\text{imp}\,nn'}(E) = \mathcal{G}_{LL'}^{\text{host}\,nn'}(E) + \sum_{n''n'''}\sum_{L''L'''} \mathcal{G}_{LL''}^{\text{host}\,nn''}(E) \tau_{L''L'''}^{n''n'''}(E)$$

$$\times \mathcal{G}_{L'''L'}^{\text{host}\,n'''n'}(E) \quad (16)$$

in analogy to Equation (3).

As the vacuum region is geometrically described by layers of empty sites parallel to the crystal surface, it is convenient to approximate the Fourier integration over a surface at distance z by an integration over a vacuum layer of volume Ω_{scan}, centered at z: $\int d^2 r \rightarrow \sum_{n \in \Omega_{\text{scan}}} \int_n d^3 r$. Expression (10) then becomes

$$\Delta G(\boldsymbol{q}; E) = \Delta G_S(\boldsymbol{q}; E) + \Delta G_M(\boldsymbol{q}; E), \quad \text{with}$$

$$\Delta G_S(\boldsymbol{q}; E) = \sum_{j\nu}^{\Omega_{\text{scan}} \cap \Omega_{\text{imp}}} e^{-i\boldsymbol{q}\cdot(\boldsymbol{R}_j + \chi_\nu)} \int_{j\nu} d^3 x\, e^{-i\boldsymbol{q}\cdot\boldsymbol{x}}$$

$$\times \sum_L \Delta G_{S;L}^{j\nu}(\boldsymbol{x}, \boldsymbol{x}; E)$$

$$\Delta G_M(\boldsymbol{q}; E) = \frac{\Omega_{\text{BZ}}}{\Omega_{\text{rec}}^2} \sum_\nu e^{i\boldsymbol{q}\cdot\chi_\nu} \int d^2 k \sum_{i\mu, i'\mu'}^{\Omega_{\text{imp}}} e^{-i\boldsymbol{k}\cdot\boldsymbol{R}_i} e^{-i(\boldsymbol{k}-\boldsymbol{q})\cdot\boldsymbol{R}_{i'}} \quad (17)$$

$$\times \sum_{LL'L''L'''} \mathcal{G}_{LL''}^{\text{host}\,\nu\mu'}(\boldsymbol{k}; E)\tau_{L''L'''}^{i\mu;i'\mu'}(E)$$

$$\times \mathcal{G}_{L'''L'}^{\text{host}\,\mu'\nu}(\boldsymbol{k} - \boldsymbol{q}; E)$$

$$\times \int_\nu d^3 x\, e^{-i\boldsymbol{q}\cdot\boldsymbol{x}}[\mathcal{R}_L^\nu(\boldsymbol{x}; E)\bar{\mathcal{R}}_{L'}^\nu(\boldsymbol{x}; E)]$$

where we set $n = (j, \nu)$, $\Delta G_{S;L}^{j\nu}(\boldsymbol{x}, \boldsymbol{x}; E) = G_{S;L}^{\mathrm{imp};j\nu}(\boldsymbol{x}, \boldsymbol{x}; E) - G_{S;L}^{\mathrm{host};j\nu}(\boldsymbol{x}, \boldsymbol{x}; E)$ is the difference of the single-site part of the Green function between the impurity and the host system, and is taken only in the impurity region Ω_{imp} (it vanishes outside). In the aforementioned expression, the terms $[\mathcal{R}_L^\nu(\boldsymbol{x}; E)\bar{\mathcal{R}}_{L'}^\nu(\boldsymbol{x}; E)]$ and $\Delta G_{S;L}^\nu(\boldsymbol{x}, \boldsymbol{x}; E)$ are 2×2 or 4×4 matrices (depending if the Pauli–Schrödinger or the Dirac theory is used) and must be traced to form the density (Equation (2)). Conveniently, they show no $\boldsymbol{k}$-dependence and thus must be calculated only once at each energy; the same is true for the matrix elements of the scattering path operator, $\tau_{L'L''}^{i\mu;i'\mu'}(E)$. The only quantities that need to be calculated for a dense set of $\boldsymbol{k}$-points (which implies a large numerical effort) are the host structural Green functions [Equation (15)]. Fortunately, by virtue of the principal layer and decimation techniques,[15–17] the latter can be computed with a numerical effort that grows linearly with the number of atomic layers in the film, making possible the accurate simulation of the QPI in thick films (of the order of hundreds of atomic layers, if necessary) or semi-infinite geometries.

If we wish to calculate the quantity $\Delta\check{n}(z; \boldsymbol{q}; E)$ [Equation (13)], i.e., exclude the impurity and its immediate surroundings [indicated by Ω_{excl} in Equation (13)] from the Fourier transformation, then Equation (17) changes. The single-site term, ΔG_S, vanishes automatically outside Ω_{imp}. However, we must also explicitly subtract the contribution of the multiple-scattering term in Ω_{excl}. The result is given by replacing $\Delta G_S(\boldsymbol{q}; E)$ by the following correction to the multiple scattering part

$$
\begin{aligned}
\mathcal{C}_M(\boldsymbol{q}; E) = &\sum_{j\nu}^{\Omega_{\mathrm{excl}}} e^{-i\boldsymbol{q}\cdot(\boldsymbol{R}_j+\chi_\nu)} \sum_{i\mu, i'\mu'}^{\Omega_{\mathrm{imp}}} \sum_{LL'L''L'''} \mathcal{G}_{LL''}^{\mathrm{host}\,j\nu;i\mu}(E) \tau_{L'L'''}^{i\mu,i'\mu'} \\
&\times \mathcal{G}_{L'''L'}^{\mathrm{host}\,i'\mu';j\nu}(E) \times \int_{i\nu} d^3x\, e^{-i\boldsymbol{q}\cdot\boldsymbol{x}}[\mathcal{R}_L^\nu(\boldsymbol{x}; E)\bar{\mathcal{R}}_{L'}^\nu(\boldsymbol{x}; E)]
\end{aligned}
\tag{18}
$$

For the calculation of the integrals $\int_\nu d^3x\, e^{-i\boldsymbol{q}\cdot\boldsymbol{x}}[\mathcal{R}_L^\nu(\boldsymbol{x}; E)\bar{\mathcal{R}}_{L'}^\nu(\boldsymbol{x}; E)]$, we expand the wavefunctions in spherical harmonics, as is normally done in the KKR method,[18] and we do the same for the exponential by the identity $e^{-i\boldsymbol{q}\cdot\boldsymbol{x}} = 4\pi \sum_{lm} i^l j_l(qx) Y_{lm}(\hat{\boldsymbol{k}}) Y_{lm}^*(\hat{\boldsymbol{x}})$, where Y_{lm} are spherical harmonics. Thus the integral is decomposed in a spherical and an angular part. The integrals containing irregular functions that contribute to $\Delta G_{SL}(\boldsymbol{q}; E)$ are handled in an analogous way.

In summary, in the KKR method, we calculate the quantities $\Delta n(\boldsymbol{q}; E)$ [Equation (11)] and $\Delta\check{n}(\boldsymbol{q}; E)$ [Equation (13)] by

$$
\begin{aligned}
\Delta n(\boldsymbol{q}; E) = -\frac{1}{2i\pi} \mathrm{Tr}[&\Delta G_M(\boldsymbol{q}; E) - \Delta G_M(-\boldsymbol{q}; E)^* \\
&+ \Delta G_S(\boldsymbol{q}; E) - \Delta G_S(-\boldsymbol{q}; E)^*]
\end{aligned}
\tag{19}
$$

$$
\Delta\check{n}(\boldsymbol{q}; E) = \Delta n(\boldsymbol{q}; E) + \frac{1}{2i\pi} \mathrm{Tr}[\mathcal{C}_M(\boldsymbol{q}; E) - \mathcal{C}_M(-\boldsymbol{q}; E)^*]
\tag{20}
$$

2.3. Multiple Scattering among Impurities

The experimental QPI Fourier transform is usually performed over a large surface area comprising many impurities. A direct simulation of this experiment should account for the contribution of the multiple-scattering events between impurities to the QPI. However, this is numerically expensive, as it involves the calculation of a large $\mathcal{T}$-matrix, corresponding to the collection of all impurities in a large supercell, and perhaps even a statistical average over many impurity configurations. Fortunately, the Fourier-transformed QPI of a single impurity is an excellent approximation to the result of a random impurity distribution, simplifying the calculations. Fang et al.[19] have shown this approximation to hold to lowest order in the potential difference ΔV, i.e., in the Born approximation to the scattering amplitude. Here, we argue that the approximation holds in general, allowing for the treatment of strong, e.g., resonant, scattering.

First, we discuss the form of the multiple-scattering $\mathcal{T}$-matrix. Let $t_n(E)$ be the $\mathcal{T}$-matrix of a single impurity at site n and expressed in a matrix form in a localized basis set. Then, the full $\mathcal{T}$-matrix of a collection of impurities obeys the expansion[20]

$$
\begin{aligned}
\mathcal{T}_{nn'} = &t_n\delta_{nn'} + t_n G_{nn'}^{\mathrm{host}}(1 - \delta_{nn'})t_{n'} \\
&+ \sum_{m \neq n, n'} t_n G_{nm}^{\mathrm{host}} t_m G_{mn'}^{\mathrm{host}} t_{n'} + \cdots
\end{aligned}
\tag{21}
$$

$$
= t_n\delta_{nn'} + t_n \sum_m \check{G}_{nm} \mathcal{T}_{mn'}
\tag{22}
$$

where the matrix $\check{G}_{nm} = G_{nm}^{\mathrm{host}}(1 - \delta_{nm})$ contains the site-off-diagonal part of the Green function (a proof is given in the Appendix). The aforementioned expression includes all multiple-scattering events among impurities, while avoiding sequential scattering off the same impurity (as t_n contains the sequential site-diagonal scattering to all orders of ΔV).

We assume that the impurities are nonoverlapping (which is a reasonable approximation at low concentration) and identical and are thus characterized by the same matrix $t_n = t\,\forall n$. We also apply in part the stationary phase approximation for the host Green function,[6] which is valid at long distances. This is justified at low impurity concentrations as the largest part of the surface, where the Fourier transform is performed, is covered by host atoms and is far from the impurities. Within this approximation, the host Green function may be approximated by $G^{\mathrm{host}}(\boldsymbol{R}_n + \boldsymbol{x}, \boldsymbol{R}_{n'} + \boldsymbol{x}'; E) = K_{nn'}(\boldsymbol{x}, \boldsymbol{x}'; E)e^{i\boldsymbol{k}_{nn'}\cdot\boldsymbol{R}_{nn'}}$, where $\boldsymbol{k}_{nn'}$ is a stationary point on the constant energy surface $E_{\boldsymbol{k}_{nn'}} = E$, and is defined by the property that the group velocity $\boldsymbol{v}_{\boldsymbol{k}_{nn'}}$ must be parallel to the vector $\boldsymbol{R}_{nn'} = \boldsymbol{R}_n - \boldsymbol{R}_{n'}$. The quantity $K_{nn'}(\boldsymbol{x}, \boldsymbol{x}'; E)$ contains the rest of the Green function, including a power–law decay with distance ($K_{nn'} \propto |\boldsymbol{R}_{nn'}|^{-1/2}$ in two dimensions). The important consequence of this approximation for our purposes is that the phase of the long-distance propagation, $e^{i\boldsymbol{k}_{nn'}\cdot\boldsymbol{R}_{nn'}}$, is governed only by the stationary point (in the case of multiple stationary points, a summation over the corresponding contributions is implied). Then we argue that, in the Fourier transform of Equation (10), the contribution of the first term of the right-hand side of Equation (22) is dominant and equal to the single-impurity contribution, whereas the remainder (the contribution of $t\check{G}\mathcal{T}$) is negligible.

We decompose the Green function difference (Equation (3)) in two terms corresponding to the decomposition of the $\mathcal{T}$-matrix (22)

$$\Delta G_{nn} = \Delta G_{nn}^{(1)} + \Delta G_{nn}^{(2)} \tag{23}$$

$$= \sum_m G_{nm}^{\text{host}} t G_{mn}^{\text{host}} + \sum_m G_{nm}^{\text{host}} t \sum_{n'n''} \breve{G}_{mn'} \mathcal{T}_{n'n''} G_{n''n}^{\text{host}} \tag{24}$$

All first-order terms, $G_{nm}^{\text{host}} t G_{mn}^{\text{host}}$, give identical contributions to the Fourier transform $\Delta G(q)$, because both G_{mn}^{host} and G_{nm}^{host} depend on the sites n and m only via the difference R_{nm}. If N is the number of impurities, and setting one impurity at position $m = 0$, we have $\sum_n \int_n d^2 x e^{-iq\cdot(x+R_n)} \sum_m G_{nm}^{\text{host}} t G_{mn}^{\text{host}} = N \sum_n \int_n d^2 x e^{-iq\cdot(x+R_n)} G_{n0}^{\text{host}} t G_{0n}^{\text{host}}$, which can be shown by changing the summation over R_m to R_{nm}. This is, however, not true for the higher-order terms. Applying the stationary phase approximation to $G_{n''n}^{\text{host}}$ in Equation (24) (last term), we obtain $\Delta G_{nn}^{(2)} = \sum_m G_{nm}^{\text{host}} t \sum_{n'n''} \breve{G}_{mn'} \mathcal{T}_{n'n''} K_{n''n} e^{ik_{n''n}\cdot R_{n''n}}$. In the Fourier transformation, the translational symmetry of the host allows us again to place $m = 0$ by a reindexing, but the contribution of the last phase, $e^{ik_{n''n}\cdot R_{n''n}}$, cannot be lifted. As the impurities are randomly placed, the total contribution of the random phases over all impurities practically cancels in the Fourier transform. Of course, an exact cancellation requires a sum over all configurations and thus cannot take place unless the scanned surface area is infinitely large, which is never the case. However, our analysis shows that the single-site term should always give the dominant contribution. In this respect, a calculation of the single-impurity Fourier transform should give a qualitatively and quantitatively representative picture of the full problem, which is numerically advantageous in an ab initio calculation.

We tested our hypothesis in a model system of a free-electron surface with s-wave-scattering point defects, randomly placed and averaged over 50 configurations. Numerical simulations (not shown here) of 1000 impurities in a $1000 \times 1000 \,\text{Å}^2$ box show that, in the Fourier transform, the single-site term dominates over the multiple-scattering contribution by an order of magnitude.

2.4. Joint Density of States: Ad Hoc Model or Approximation?

A frequently used approach to the Fourier-transformed QPI is the joint density of states (JDOS)[4,7,21,22] or extended JDOS (exJDOS)[23] approach, which is applied if the constant-energy contours (CECs) $\{k | E_k = E\}$ at energy E are known (e.g., from calculations or from angular-resolved photoemission experiments), but the full Green function G^{host} or the full $\mathcal{T}$-matrix are not known. Motivated by Equation (10), one defines the quantity

$$\text{exJDOS}(q; E) = \int_{E_k = E} dk\, n_{\text{surf}}(k; E) M_{k,k-q} \gamma_{k,k-q}^{\text{STM}} n_{\text{surf}}(k - q; E) \tag{25}$$

which a weighted convolution of the spectral amplitude at the pristine crystalline surface, $n_{\text{surf}}(k; E) = \int_{\text{surf}} |\Psi_k(r)|^2 d^3 r$ (the integration over r takes place in the surface and/or in the vacuum region where the STM is positioned). Here, k and $k - q$ are confined to the CEC by assumption. The matrix element $M_{k,k-q}$ contains information on the scattering properties of the defect. For topological insulators, where spin-flip

scattering is at the center of interest, and for nonmagnetic defects, where spin-flip scattering is suppressed, the reasonable approximation $M_{k,k-q} = |\mathcal{T}_{k,k'}|^2 \propto 1 + \cos(s_k, s_{k'})$ has been proposed[4], where s_k is the spin polarization vector of the state at k. In addition, a factor $\gamma_{k,k-q}^{\text{STM}} = 1 - \cos(v_k, v_{k-q})$ was introduced in the study by Sessi et al.[23] to promote standing wave formation by back-scattering (opposite group velocities), in the spirit of the stationary phase approximation. At the end, $\text{exJDOS}(q; E)$ is expected to approximately reproduce $|\Delta n(q; E)|$, as both should peak at the scattering vectors.

The JDOS approach has been introduced as an ad hoc model. The question is if it also constitutes an approximation to the theory expressed by Equation (7), (10), and (11). We find that $\text{exJDOS}(q; E) \propto |\Delta n(q; E)|^2$, under a number of assumptions that are scrutinized in the following. From Equation (10) and (11), we have (dropping the variables E and z)

$$|\Delta n(q)|^2 = \Delta n(q) \Delta n(-q) = -\frac{1}{4\pi^2} \text{Tr}[\Delta G(q) - \Delta G(-q)^*] \\ \times \text{Tr}[\Delta G(-q) - \Delta G(q)^*] \tag{26}$$

We use the stationary phase approximation to the Green function, according to which

$$\Delta G(r, r; E) = -\frac{4\pi^3}{\Omega_{\text{rec}}^2 \hbar^2} \sum_{k(r), \bar{k}(r)} u_k(r) \mathcal{T}_{k,\bar{k}} u_k^\dagger(r)$$

$$\times \exp\left\{ -\frac{i\pi}{4} \left[\text{sign}\left(\frac{\partial^2 E_k}{\partial k_\parallel^2} \right) + \text{sign}\left(\frac{\partial^2 E_{\bar{k}}}{\partial \bar{k}_\parallel^2} \right) \right] \right\} \tag{27}$$

$$\times (|v_k||v_{\bar{k}}|)^{-1/2} \left| \frac{\partial^2 E_k}{\partial k_\parallel^2} \frac{\partial^2 E_{\bar{k}}}{\partial \bar{k}_\parallel^2} \right|^{-1/2} \frac{e^{i(k-\bar{k})\cdot r}}{|r|}$$

$$= \sum_{k\bar{k}} a_k a_{\bar{k}} u_k(r) \mathcal{T}_{k,\bar{k}} u_{\bar{k}}^\dagger(r) e^{i(k-\bar{k})\cdot r} / |r| \tag{28}$$

at large distances $|r|$ from the impurity (which is placed at $r = 0$). We omitted the band index α to simplify the notation. The discrete summation for a given r in (27) runs over k-points that are stationary with respect to the host Green function phase, i.e., they are pinned with respect to the energy, $E_k = E_{\bar{k}} = E$, and also pinned at such positions on the CEC, that the group velocity v_k is in the direction r and the group velocity $v_{\bar{k}}$ is in the opposite direction, $-r$. The symbols u_k and $u_{\bar{k}}$ stand for the lattice-periodic part of the wave-function, whereas $k_\parallel$ and $\bar{k}_\parallel$ run on the CEC. The last expression (28) is a convenient abbreviation with obvious shorthand notation for a_k and $a_{\bar{k}}$. The Fourier transformation reads

$$\Delta G(q; E) = \int d^2 r \sum_{k\bar{k}} a_k a_{\bar{k}} u_k(r) \mathcal{T}_{k,\bar{k}} u_{\bar{k}}^\dagger(r) e^{i(k-\bar{k}-q)\cdot r} / |r| \tag{29}$$

$$= \int_0^\infty dr \sum_{\text{CEC}} \int_{\text{CEC}} dk_\parallel \mathcal{D}(k_\parallel) \sum_{\bar{k}} a_k a_{\bar{k}} u_k(r) \\ \times \mathcal{T}_{k,\bar{k}} u_{\bar{k}}^\dagger(r) e^{i(k-\bar{k}-q)\cdot r} \tag{30}$$

In the last step, we converted the integration variable from $d^2 r$ to $r dr d\theta$ and subsequently $d\theta$ to $\mathcal{D}(k_\parallel) dk_\parallel$, where the variable $k_\parallel$ is a parameter running over all CECs as θ forms the unit

circle (to each stationary point $\boldsymbol{k}$ corresponds a direction θ). The quantity $\mathcal{D}(k_\parallel)$ is the integration weight corresponding to the latter transformation and depends on the exact shape of the CEC. The stationary points $\boldsymbol{k}$ and $\bar{\boldsymbol{k}}$ are now functions of $k_\parallel$ on the CEC, instead of θ (essentially $\boldsymbol{k}$ coincides with $k_\parallel$ on the CEC). To each $\boldsymbol{k}$, there may correspond multiple $\bar{\boldsymbol{k}}$ points of opposite group velocity, therefore the summation over multiple possible $\bar{\boldsymbol{k}}$ for each $k_\parallel$ remains.

So far we have only used the stationary phase approximation. To derive the JDOS or the exJDOS model, we must make additional assumptions. First, the weight $\mathcal{D}(k_\parallel)$ must be dropped, or set to a constant, as it does not appear in the exJDOS expression. But this is justifiable only when the CEC is approximately isotropic. Then, the assumption must be made that the dominant contribution to the Fourier transform of Equation (30) comes from the points where the phase vanishes ($\boldsymbol{k} - \bar{\boldsymbol{k}} - \boldsymbol{q} = 0$), dropping the r-integration and confining the $k_\parallel$-integration only to the points satisfying the latter condition. In addition, on forming products of the type $G(\boldsymbol{q}; E)G(\boldsymbol{q}; E)^*$ (and similar) that occur in Equation (26), products of wavefunctions of the type $u_{\boldsymbol{k}}^\dagger u_{\boldsymbol{k}'}$ expressing the density, as well as products of $\mathcal{T}$-matrix elements expressing the transition rate, will appear. To comply with the JDOS (25), the mixed-$\boldsymbol{k}$ (i.e., $\boldsymbol{k} \neq \boldsymbol{k}'$) density terms must be dropped. The terms $a_{\boldsymbol{k}}$ and $a_{\bar{\boldsymbol{k}}}$ should be also ignored (or set to a constant). Finally, the weighting factor $\gamma_{\boldsymbol{k},\boldsymbol{k}-\boldsymbol{q}}^{\text{STM}} = \delta\left(\frac{v_{\boldsymbol{k}}}{|v_{\boldsymbol{k}}|} + \frac{v_{\boldsymbol{k}-\boldsymbol{q}}}{|v_{\boldsymbol{k}-\boldsymbol{q}}|}\right)$ (instead of the milder $\gamma_{\boldsymbol{k},\boldsymbol{k}-\boldsymbol{q}}^{\text{STM}} = 1 - \cos(v_{\boldsymbol{k}}, v_{\boldsymbol{k}-\boldsymbol{q}})$) should be set in the definition of the exJDOS (25) to account for the stationary-phase approximation.

The aforementioned discussion shows that the JDOS and exJDOS approaches are not quantitative approximations but qualitative models. Still, they comprise the essential parts of the information that one usually seeks in Fourier-transformed QPI spectra and therefore constitute a useful tool for their analysis.

3. Applications

To showcase the use of our newly developed method, we apply it to the topological insulator Bi_2Te_3, which hosts nontrivial surface states characterized by spin-momentum locking that are protected by time-reversal symmetry against backscattering.

In our density functional calculations within the relativistic full-potential KKR Green function framework,[24–27] we considered a six quintuple layer thick film of Bi_2Te_3 using the experimental lattice constant,[28] which was chosen such that the "top" and "bottom" surface states of the thin film decouple. We used an angular momentum cutoff of $\ell_{\max} = 3$ including corrections for the exact shape of the cells[29,30] and the local spin density approximation[31] for the exchange-correlation functional. The Fermi level was set such that it resides inside the bulk band gap, which ensures that the Fermi surface consists of the topological surface state alone without projections of bulk bands. Such a situation can be achieved experimentally by doping or gating. **Figure 1** shows the setup of the calculation, where the bandstructure (Figure 1a) and Fermi surface of the system at hand (Figure 1b) are shown together with the spin-polarization of the topological surface state. Our calculations reproduce the experimentally measured warping of the Fermi surface for bulk

insulating samples[33] reasonably well. For a better quantitative agreement of the size of bulk bandgap and the strength of the warping, more demanding calculations using the GW approximation[34,35] would be needed which is beyond the scope of this work.

Single substitutional impurities were embedded into the Bi_2Te_3 host at the outermost Bi site, as shown in Figure 1c. We considered nonmagnetic Te_{Bi} (the subscript indicates the substituted position) defect, which occurs naturally as an antisite defect, as well as magnetic Mn_{Bi} and Fe_{Bi} impurity atoms. It has been previously shown[36–38] that the substitutional Bi site is a thermodynamically stable position of transition metals in Bi_2Te_3, indicating the relevance of our findings. The impurities were embedded into the host system self-consistently making use of the Dyson equation[25] while neglecting structural relaxations around the impurities. The first shell of nearest neighbors was included in the calculation for a correct screening of the charge of the impurities. The resulting density of states for the three defects are shown in Figure 1d. Although the density of states at the Fermi level is small for the Te_{Bi} defect, the incompletely filled d shell of the transition metal impurities results in a higher density of states at the Fermi level. In accordance to Hund's rule, we find that the Mn_{Bi} defect is close to half-filling, whereas the Fermi level bisects the d state resonance of the Fe_{Bi} impurity. From analyzing the impurity density of states and in the spirit of the Friedel sum rule, which was recently demonstrated to hold in this class of materials,[39] one expects considerable differences in the scattering properties of the different impurities. In addition, the magnetic nature of the Mn and Fe defects is expected to reopen the forbidden backscattering channel due to the breaking of time-reversal symmetry.

The strong hexagonal warping in Bi_2Te_3 leads to a snowflake-like shape of the Fermi surface that enables two major scattering channels,[12,40] $\boldsymbol{q}_1$ and $\boldsymbol{q}_2$, which are shown in Figure 1e. The backscattering channel ($\boldsymbol{q}_1$) is expected to be suppressed by time-reversal symmetry for scattering off nonmagnetic defects and can be reopened by scattering off magnetic defects. The trivial scattering channel $\boldsymbol{q}_2$ is however always possible. These facts are illustrated by the JDOS [Equation (25) with $M_{\boldsymbol{k},\boldsymbol{k}'} = \gamma_{\boldsymbol{k},\boldsymbol{k}'}^{\text{STM}} = 1$] and spin-conserving JDOS (SJDOS, $M_{\boldsymbol{k},\boldsymbol{k}'} = \boldsymbol{s}_{\boldsymbol{k}} \cdot \boldsymbol{s}_{\boldsymbol{k}'}$, $\gamma_{\boldsymbol{k},\boldsymbol{k}-\boldsymbol{q}}^{\text{STM}} = 1$) shown in Figure 1f,g, which reveal that the suppression of backscattering introduced by forbidden time-reversal scattering suppresses the signal at $\boldsymbol{q}_1$ (Figure 1g). The suppression of the signal at $\boldsymbol{q}_1$ is however incomplete because the backscattering contribution highlighted with the red arrow in Figure 1e is not the only contribution to the QPI signal at this $\boldsymbol{q}$-point. Additional contributions coming from vectors $\boldsymbol{q}_{1'}$ at $k_\gamma = \pm 0.07\text{Å}^{-1}$ in Figure 1e, where the suppression with the factor $\boldsymbol{s}_{\boldsymbol{k}} \cdot \boldsymbol{s}_{\boldsymbol{k}'}$ is incomplete, overshadow the suppression partially. It should be noted that the widely used JDOS and SJDOS approaches use only information about the electronic structure of the host system while neglecting the scattering properties of the impurities except for their ability to conserve or break time-reversal symmetry. In the following sections, the analogous results for the improved impurity-specific Fourier-transformed QPI (FT-QPI) simulation within the KKR formalism that considers the scattering properties of the impurities will be discussed and compared with the standard (S)JDOS approaches.
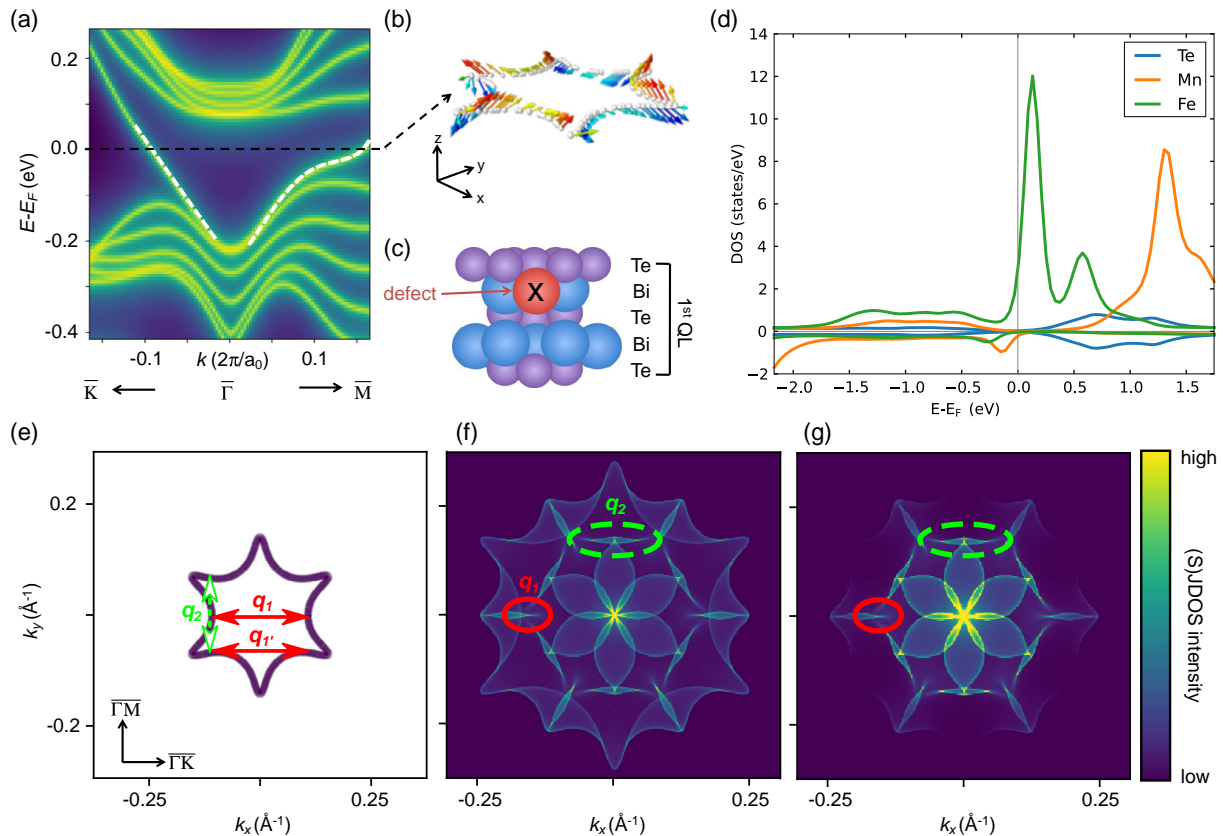
Figure 1. Setting of the numerical simulations. a) Bandstructure of Bi_2Te_3 with the topological surface state highlighted with white dashed lines and b) its spin polarization on the Fermi surface. c) Location of the substitutional impurities in the outer most Bi layer and d) the density of states (DOS) of the different impurities under consideration (the positive DOS axis corresponds to spin-up, the negative to spin-down). e) Hexagonally warped Fermi surface of Bi_2Te_3 with the most prominent scattering channels, q_1 and q_2, indicated by solid red and dashed green arrows, respectively. f) JDOS and g) SJDOS show the conventional way of interpreting FT-QPI images. Adapted under the terms of a Creative Commons Attribution CC BY 4.0 license.[32] Copyright 2018, The Author, published by Forschungszentrum Jülich.

3.1. Impurity Specific FT-QPI from First Principles

The main calculations of this work are shown in **Figure 2**. Figure 2a shows the real-space oscillations in the charge density on the surface, induced by a single subsurface Mn_{Bi} impurity, often referred to as Friedel oscillations. The change in the charge density on the surface was computed for 2148 atomic positions within a radius of 108 Å around the position of the impurity. Note that supercell-based approaches would have to deal with a size of approximately $50 \times 50 \times 30 = 75\,000$ atoms in the unit cell. To demonstrate the validity of our following simulations, we conducted a fast Fourier transform (FFT) of the real-space data, which is shown in Figure 2b. The FT-QPI image is dominated by the near-impurity region, resulting in a strong background centered around $q = 0$. To reveal the scattering signatures visible in the long-range tail of the Friedel oscillations around the impurity, we furthermore substracted the near-impurity region within a radius of 7.2 Å from the FFT (excluding explicitly the first four shells of neighbors), as it is frequently done[11] in QPI analyses of STM experiments. The result is shown in Figure 2c, where we identify signatures of the two dominant scattering channels, q_1 and q_2, in the resulting image as well as a star-like feature

[highlighted by six white lines in Figure 2c] associated to small angle-scattering off the impurities. Although this FFT comprises a very large region around the impurity only a low resolution could be achieved in the resulting image. It is obvious that for sufficient accuracy much larger regions need to be included in the FFT, which is, however, numerically expensive.

The results of out new implementation are shown in Figure 2d–f for the full Fourier transform of the Te_{Bi}, Mn_{Bi}, and Fe_{Bi} impurities, respectively. The images were simulated using a dense k-point mesh of 301×301 points in the Brillouin zone with a broadening introduced by a small imaginary part in the energy of ≈ 5 meV. The results were checked to be converged with respect to these numerical parameters. The much higher resolution in the full FT-QPI images (Figure 2d–f) reveal clear evidence of the prominent q_1- and q_2-signals, which are far better resolved when the same near-impurity regions including the first four shells around the impurity position is excluded from the Fourier transform (Figure 2g–i).

Next, we compare the different signatures (intensities at q_1, q_2) in the FT-QPI image among the different impurities. Scattering off the nonmagnetic Te_{Bi} defect is characterized by a strong focus
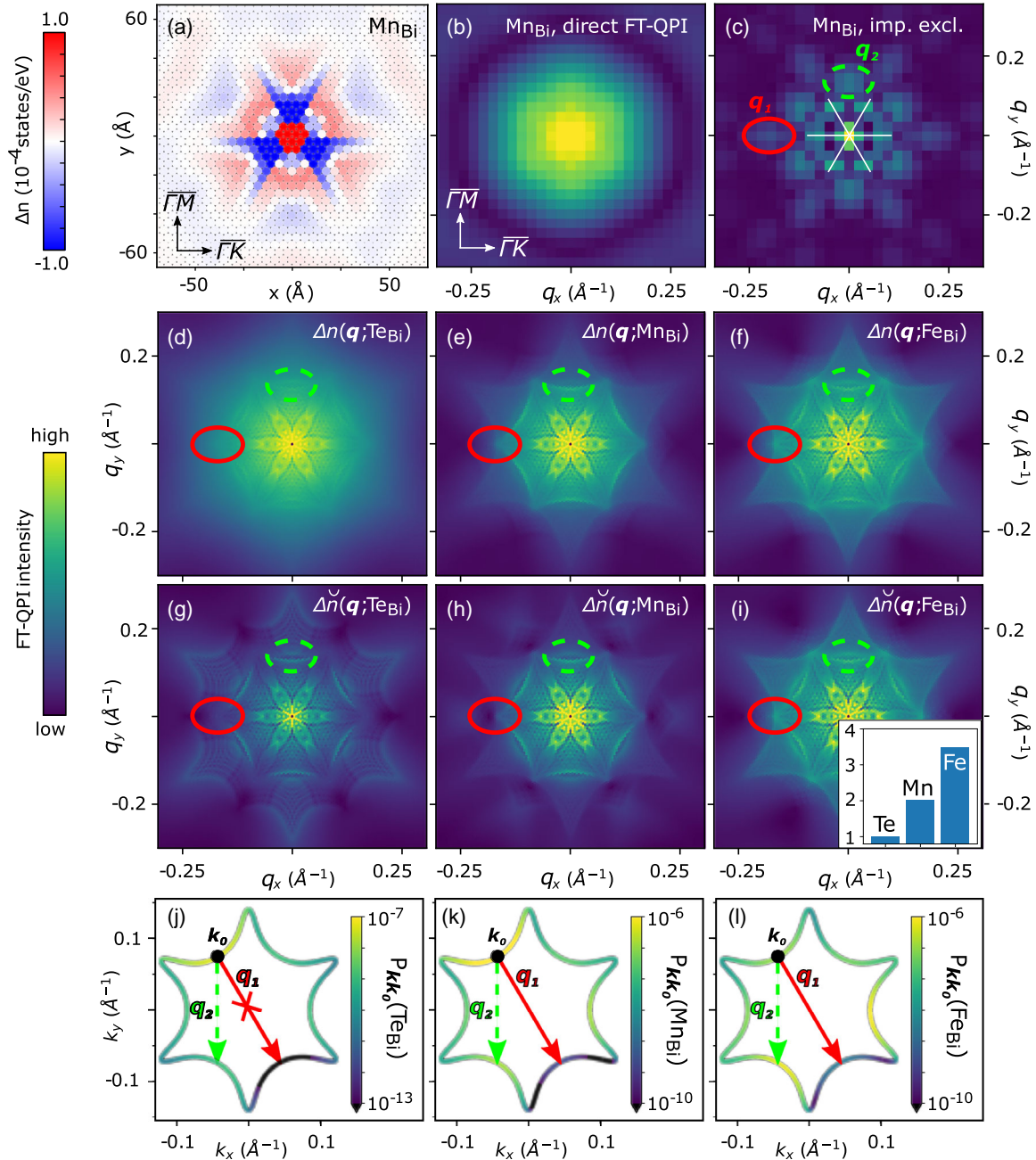
Figure 2. QPI from first principles. a) Real-space image of the charge density oscillations integrated within atomic cells at a distance of $z = 1.4\,\text{Å}$ above a Mn_{Bi} impurity situated at $(0,0)$. b) FT-QPI of of the real-space data shown in (a) computed via FFT. c) FT-QPI as in (b) but with the near-impurity region within a radius of $R_0 = 10\,\text{Å}$ (including up to fourth nearest neighbors) set to zero. d–f) Impurity specific FT-QPI images [after Equation (11)] for Te_{Bi}, Mn_{Bi}, and Fe_{Bi} impurities. g–i) Corresponding FT-QPI images excluding the near-impurity region within R_0 [after Equation (13)] as in (c). j–l) Scattering rate (P_{k,k_0} in $1/(\text{fs at\% d}L)$ with dL being the Fermi surface line segment) on the Fermi surface for an incoming wave characterized by the wavevector k_0 for scattering off the Te_{Bi}, Mn_{Bi}, and Fe_{Bi} impurities, respectively. The inset in (i) shows the ratio of the FT-QPI intensity at q_1 in (g–i) relative to the signal of the Te_{Bi} impurity ($\Delta \breve{n}(q_1)/\Delta \breve{n}(q_1; Te_{Bi})$). Adapted under the terms of a Creative Commons Attribution CC BY 4.0 license.[32] Copyright 2018, The Author, published by Forschungszentrum Jülich.

in forward (i.e., small-angle or $q = 0$) scattering direction. This is a consequence of the forbidden backscattering that disallows the scattering vector q_1 as seen by looking at the scattering rate $P_{k,k_0} = \frac{2\pi}{\hbar}|\mathcal{T}_{k,k_0}|^2 \delta(E_k - E_{k_0})$,[24,26,27] which is illustrated for one particular incoming wave, k_0, in Figure 2j. The strong focus

to small angle scattering leads to the absence of a signal at q_1 and only a moderate intensity at q_2 compared with the dominant star-like feature around $q = 0$. In contrast, the intensity at q_2 is stronger for the Mn_{Bi} and Fe_{Bi} impurities (Figure 2h,i). This is a consequence of the lesser focused scattering in forward

direction, as shown in Figure 2k,l for the Mn_{Bi} and Fe_{Bi} impurities. It should, however, be noted that the overall scattering strength is roughly ten times larger for the Mn and Fe impurities compared with Te (see color scales in Figure 2j–l), which leads to a more pronounced start-like central feature in the QPI images around $q = 0$ in (Figure 2h) compared with (Figure 2g). Although the magnetic impurities break the protection against backscattering, the backscattering amplitude is still much smaller than scattering into forward direction or near $120°$-scattering (q_2). This results in the relatively weak signal of backscattering (q_1) in the FT-QPI image of single magnetic defects. This result is in line with recent investigations in Mn-doped Bi_2Te_3, where ferromagnetically coupled clusters of atoms were shown to be necessary for the efficient reopening of the backscattering channel within the topological surface state.[23] The higher backscattering rate off the Fe_{Bi} impurity (see the amplitude of P_{-k_0, k_0} in Figure 2l) compared with the Mn_{Bi} defect (Figure 2k) seems counter intuitive at first sight when considering that Mn has the higher spin moment ($4.48 \mu_B$) compared with Fe ($3.54 \mu_B$). However, considering the higher density of states at the Fermi level in the case of the Fe_{Bi} impurity in the context of Wigner's time delay, which relates the higher scattering potential to a longer effective stay at the impurity, the more efficient coupling of the surface state electrons in Bi_2Te_3 to the Fe_{Bi} impurity becomes apparent. As a consequence the FT-QPI intensity at q_1 in fact increases by a factor ≈ 2 and ≈ 3.5 (see inset in Figure 2i), when going from Te_{Bi} over Mn_{Bi} to the Fe_{Bi} defect, which is a clear signature of the increasing backscattering amplitude.

A comparison of our simulations to experimental results for nonmagnetic (Ca doping) and magnetic (Mn) doping of Bi_2Te_3[12] shows a good agreement between theory and experiment. The two main features (i.e., high intensity around $q = 0$ and the 6 features at q_2) are well reproduced. It can however be seen that our simulations show more structure in the resulting QPI images which we attribute to different effects that are omitted in the simulation. Possible reasons why the experimental pictures are more smeared out are local fluctuations of the Fermi level, additional impurity configurations like adatoms or intrinsic defects such as vacancies or antisites.

In summary, our simulations of the impurity-specific FT-QPI reveals that not only information on the host's electronic structure can be extracted but also the scattering properties of different impurities are accessible.

3.2. Comparison with JDOS Approaches

Usually the interpretation of experimental FT-QPI images is done by comparison with calculations based on the joint density of states. The comparison between the (S)JDOS in Figure 1f,g on the one hand and the impurity-specific results of the FT-QPI shown in Figure 2 on the other hand reveals that a proper description of the impurity scattering is crucial for quantitative understanding of the scattering process off defects. In particular, the intensity at the backscattering signal (q_1) is overestimated in the simple (S)JDOS approaches and the strong focus in small-angle scattering is underestimated. A significant improvement was the exJDOS (Equation (25)), that does include the correct scattering information of the different impurities and which is shown for the three defects (Te_{Bi}, Mn_{Bi}, and Fe_{Bi}) in **Figure 3**. Qualitatively, the correct FT-QPI can be reproduced and a strong suppression of the q_1 signal is found in accordance to the results of Figure 2.

This gives an a posteriori justification of the use of the exJDOS model in the interpretation of experimental QPI images and allows for the extraction of scattering information as the interplay between the electronic structure of the host system and the embedded impurities. It can, however, not be excluded that in other systems, the terms that are dropped in the JDOS-approaches (e.g., mixed k contributions or anisotropic scattering rate) become important.

4. Conclusions

We have derived a Green function and $\mathcal{T}$-matrix-based formalism for the calculation of Fourier-transformed QPI images that are measured with STM. We have implemented our theory into the KKR Green function method, allowing for ab-initio calculations for the translational-invariance-breaking impurity problem. Different from simple JDOS models, our approach accounts for the calculated scattering amplitude of the Bloch wavefunctions off the defects. We have examined the derivation of the JDOS approaches and shown that they are not quantitative
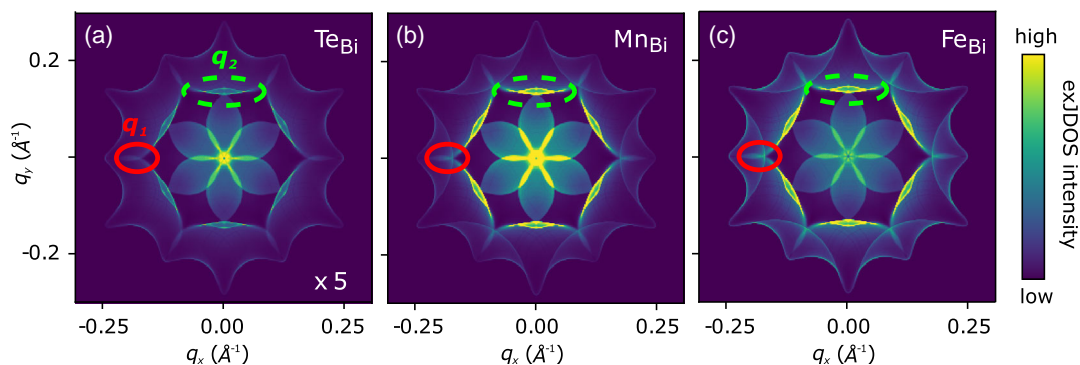
Figure 3. The exJDOS approach for the simulation of FT-QPI images of a) Te_{Bi}, b) Mn_{Bi}, and c) Fe_{Bi} impurities. A good qualitative agreement with the simulations of $\Delta \check{n}(q; E)$ in Figure 2g–i is shown, which is a significant improvment over the (S)JDOS images shown in Figure 1. Adapted under the terms of a Creative Commons Attribution CC BY 4.0 license.[32] Copyright 2018, The Author, published by Forschungszentrum Jülich.

approximations, but ad hoc qualitative models. Still, in their simplicity, they comprise an important qualitative part of the Fourier-transformed QPI physics. We have also derived the approximation of calculating the Fourier-transformed QPI from a single defect, compared with the result of multiple, randomly placed defects and shown that it is reliable at low defect concentrations because of a cancellation of the multiple-scattering wavefunction phase.

We have applied our KKR-based implementation to nonmagnetic and magnetic defects embedded in the surface of the topological insulator Bi_2Te_3, providing microscopic insights into the scattering properties of topological surface state electrons and their response to time-reversal conserving or breaking defects.

In the future, the newly developed QPI program can thus be applied to other systems than topological insulators. In particular, the study of topological materials like type-I[41] and type-II Weyl semimetals[42] benefit from QPI investigations as they allow to study the extraordinary surface states in these materials.

Appendix

Multiple-Scattering $\mathcal{T}$-Matrix

Here, we provide a proof of Equation (22) that avoids the infinite-series expansion given in the study by Rodberg and Thaler.[20] The Dyson equation for the $\mathcal{T}$-matrix can be written in two equivalent forms

$$\mathcal{T} = \Delta V + \Delta V G^{host}\mathcal{T} = \Delta V + \mathcal{T} G^{host}\Delta V \tag{A1}$$

We rewrite the first form as

$$\Delta V = \mathcal{T}(1 + G^{host}\mathcal{T})^{-1} \tag{A2}$$

Let us denote the impurity sites with the index n. It is convenient to use a notation where we collect the single-site $\mathcal{T}$-matrices in a site-diagonal matrix $\mathcal{T}_d$ with $(\mathcal{T}_d)_{nn'} = t_n\delta_{nn'}$. In analogy, we collect the diagonal part of the Green function in the matrix $(G_d^{host})_{nn'} = G_{nn}^{host}\delta_{nn'}$. ΔV is trivially site diagonal. Then, for the site-diagonal parts, we use the second form of Equation (A1) that yields $\mathcal{T}_d = \Delta V + \mathcal{T}_d G_d^{host}\Delta V$, i.e.

$$\Delta V = (1 + \mathcal{T}_d G_d^{host})^{-1}\mathcal{T}_d \tag{A3}$$

Eliminating ΔV in (A2) and (A3), we obtain

$$\mathcal{T} = \mathcal{T}_d + \mathcal{T}_d(G^{host} - G_d^{host})\mathcal{T} \tag{A4}$$

which is equivalent to (22).

Acknowledgements

Conflict of Interest

The authors declare no conflict of interest.

Keywords

[1] M. F. Crommie, C. P. Lutz, D. M. Eigler, *Nature* **1993**, *363*, 524.
[2] Y. Hasegawa, Ph Avouris, *Phys. Rev. Lett.* **1993**, *71*, 1071.
[3] L. Petersen, P. T. Sprunger, Ph Hofmann, E. Lægsgaard, B. G. Briner, M. Doering, H.-P. Rust, A. M. Bradshaw, F. Besenbacher, E. W. Plummer, *Phys. Rev. B* **1998**, *57*, R6858.
[4] P. Roushan, J. Seo, C. V. Parker, Y. S. Hor, D. Hsieh, D. Qian, A. Richardella, M. Z. Hasan, R. J. Cava, A. Yazdani, *Nature* **2009**, *460*, 1106.
[5] W.-C. Lee, C. Wu, D. P. Arovas, S.-C. Zhang, *Phys. Rev. B* **2009**, *80*, 245439.
[6] S. Lounis, P. Zahn, A. Weismann, M. Wenderoth, R. G. Ulbrich, I. Mertig, P. H. Dederichs, S. Blügel, *Phys. Rev. B* **2011**, *83*, 035427.
[7] Q.-H. Wang, D.-H. Lee, *Phys. Rev. B* **2003**, *67*, 020511(R).
[8] JuKKR: DFT made in Jülich, https://jukkr.fz-juelich.de (accessed: February 2020).
[9] J. Tersoff, D. R. Hamann, *Phys. Rev. B* **1985**, *31*, 805.
[10] H.-M. Guo, M. Franz, *Phys. Rev. B* **2010**, *81*, 041102(R).
[11] P. Sessi, private communication.
[12] H. Beidenkopf, P. Roushan, J. Seo, L. Gorman, I. Drozdov, Y. S. Hor, R. J. Cava, A. Yazdani, *Nat. Phys.* **2011**, *7*, 939.
[13] G. Hörmandinger, *Phys. Rev. Lett.* **1994**, *73*, 910.
[14] G. Hörmandinger, *Phys. Rev. B* **1994**, *49*, 13897.
[15] E. M. Godfrin, *J. Phys.: Condens. Matter* **1991**, *3*, 7843.
[16] K. Wildberger, R. Zeller, P. H. Dederichs, *Phys. Rev. B* **1997**, *55*, 10074.
[17] M. P. López Sancho, J. M. López Sancho, J. Rubio, *J. Phys. F: Met. Phys.* **1985**, *15*, 851.
[18] N. Papanikolaou, R. Zeller, P. H. Dederichs, *J. Phys.: Condens. Matter* **2002**, *14*, 2799.
[19] C. Fang, M. J. Gilbert, S.-Y. Xu, B. A. Bernevig, M. Zahid Hasan, *Phys. Rev. B* **2013**, *88*, 125141.
[20] L. S. Rodberg, R. M. Thaler, *Introduction to the Quantum Theory of Scattering*, Academic Press, New York **1967**.
[21] J. E. Hoffman, K. McElroy, D.-H. Lee, K. M. Lang, H. Eisaki, S. Uchida, J. C. Davis, *Science* **2002**, *297*, 1148.
[22] L. Simon, C. Bena, F. Vonau, M. Cranney, D. Aubel, *J. Phys. D: Appl. Phys.* **2011**, *44*, 464010.
[23] P. Sessi, P. Rüßmann, T. Bathon, A. Barla, K. A. Kokh, O. E. Tereshchenko, K. Fauth, S. K. Mahatha, M. A. Valbuena, S. Godey, F. Glott, A. Mugarza, P. Gargiani, M. Valvidares, N. H. Long, C. Carbone, P. Mavropoulos, S. Blügel, M. Bode, *Phys. Rev. B* **2016**, *94*, 075137.
[24] S. Heers, Ph.D. thesis, RWTH Aachen University **2011**.
[25] D. S. G. Bauer, Ph.D. thesis, RWTH Aachen University **2013**.

[26] N. H. Long, P. Mavropoulos, B. Zimmermann, D. S. G. Bauer, S. Blügel, Y. Mokrousov, *Phys. Rev. B* **2014**, *90*, 064406.

[27] B. Zimmermann, P. Mavropoulos, N. H. Long, C.-R. Gerhorst, S. Blügel, Y. Mokrousov, *Phys. Rev. B* **2016**, *93*, 144403.

[28] S. Nakajima, *J. Phys. Chem. Solids* **1963**, *24*, 479.

[29] N. Stefanou, H. Akai, R. Zeller, *Comput. Phys. Commun.* **1990**, *60*, 231.

[30] N. Stefanou, R. Zeller, *J. Phys.: Condens. Matter* **1991**, *3*, 7599.

[31] S. H. Vosko, L. Wilk, M. Nusair, *Can. J. Phys.* **1980**, *58*, 1200.

[32] P. Rüßmann, Ph.D. thesis, RWTH Aachen University **2018**.

[33] Y. L. Chen, J. G. Analytis, J.-H. Chu, Z. K. Liu, S.-K. Mo, X. L. Qi, H. J. Zhang, D. H. Lu, X. Dai, Z. Fang, S. C. Zhang, I. R. Fisher, Z. Hussain, Z.-X. Shen, *Science* **2009**, *325*, 178.

[34] M. Michiardi, I. Aguilera, M. Bianchi, V. E. de Carvalho, L. O. Ladeira, N. G. Teixeira, E. A. Soares, C. Friedrich, S. Blügel, P. Hofmann, *Phys. Rev. B* **2014**, *90*, 075105.

[35] O. V. Yazyev, E. Kioupakis, J. E. Moore, S. G. Louie, *Phys. Rev. B* **2012**, *85*, 161101(R).

[36] Y. S. Hor, P. Roushan, H. Beidenkopf, J. Seo, D. Qu, J. G. Checkelsky, L. A. Wray, D. Hsieh, Y. Xia, S.-Y. Xu, D. Qian, M. Z. Hasan, N. P. Ong, A. Yazdani, R. J. Cava, *Phys. Rev. B* **2010**, *81*, 195203.

[37] M. D. Watson, L. J. Collins-McIntyre, L. R. Shelford, A. I. Coldea, D. Prabhakaran, S. C. Speller, T. Mousavi, C. R. M. Grovenor, Z. Salman, S. R. Giblin, G. van der Laan, T. Hesjedal, *New J. Phys.* **2013**, *15*, 103016.

[38] J.-M. Zhang, W. Ming, Z. Huang, G.-B. Liu, X. Kou, Y. Fan, K. L. Wang, Y. Yao, *Phys. Rev. B* **2013**, *88*, 235131.

[39] P. Rüßmann, P. Mavropoulos, S. Blügel, *J. Phys. Chem. Solids* **2019**, *128*, 258.

[40] Liang Fu, *Phys. Rev. Lett.* **2009**, *103*, 266801.

[41] R. Batabyal, N. Morali, N. Avraham, Y. Sun, M. Schmidt, C. Felser, A. Stern, B. Yan, H. Beidenkopf, *Sci. Adv.* **2016**, *2*, e1600709.

[42] C.-L. Lin, R. Arafune, R.-Y. Liu, M. Yoshimura, B. Feng, K. Kawahara, Z. Ni, E. Minamitani, S. Watanabe, Y. Shi, M. Kawai, T.-C. Chiang, I. Matsuda, N. Takagi, *ACS Nano* **2017**, *11*, 111459.